ACS APPLIED ELECTRONIC MATERIALS

pubs.acs.org/acsaelm Article

Deposition, Characterization, and Performance of Spinel $InGaZnO_4$

Hendrik F. W. Dekkers,* Michiel J. van Setten, Attilio Belmonte, Adrian V. Chasin, Subhali Subhechha, Nouredine Rassoul, Anastasia V. Glushkova, Romain Delhougne, and Gouri Sankar Kar

Cite This: *ACS Appl. Electron. Mater.* 2022, 4, 1238−1249 Read Online

ACCESS | Metrics & More | Article Recommendations | Supporting Information

ABSTRACT: Polycrystalline indium−gallium−zinc oxide (IGZO) in the spinel phase was obtained by physical vapor deposition (PVD), using reactive sputtering from an IGZO target with In/Ga/Zn = 1:1:1 composition. The initial growth of spinel IGZO is investigated by X-ray diffraction measurements after annealing the film. Deposition of spinel IGZO initially starts as a mixed amorphous/*c*-axis-aligned crystalline (CAAC) film, after which a metastable spinel IGZO is formed. Using a template of polycrystalline spinel Ga_2ZnO_4, the growth of the spinel phase is immediately achieved and enables the electrical characterization of pure spinel IGZO channels in scaled thin-film field-effect transistors. The average effective channel field-effect mobility of spinel IGZO of 50 ± 10 $cm^2/(V\ s)$ is slightly higher than amorphous IGZO in the same devices. This is in line with a slightly lower effective electron mass, as is calculated with density functional theory. The calculated total energies and band gaps have similar values to CAAC-IGZO. This metastable nature identifies spinel IGZO as an intermediate phase before the onset of CAAC-IGZO formation during PVD. Spinel IGZO is an interesting alternative to amorphous IGZO (a-IGZO) and CAAC-IGZO because of potentially higher robustness to oxygen vacancy formation.

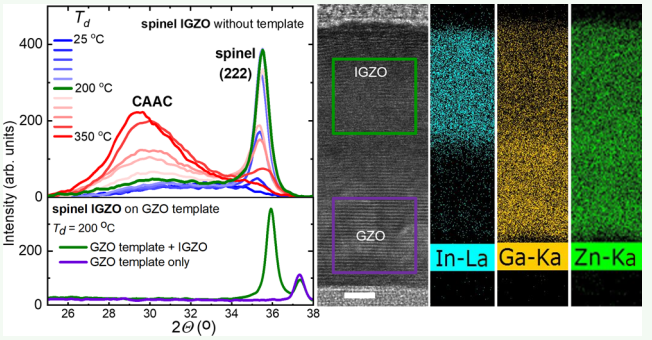

KEYWORDS: *In−Ga−Zn oxide (IGZO), Ga_2ZnO_4, spinel, c-axis-aligned crystalline (CAAC), field-effect mobility, bias stress stability*

INTRODUCTION

Oxides of the In−Ga−Zn family (IGZO) gained a lot of interest as high band gap semiconductors and are applied as channels in thin-film devices.[1] In particular, the absence of mobile holes leads to extremely low off-currents (I_{off}) in junction-free field-effect transistors,[2] enabling long charge retention times in optical display systems as well as dynamic random-access memory (DRAM) cells.[3] Since the first applications in transparent thin-film transistors (TFTs), the performance of IGZO channels is correlated with their different morphologies: crystalline and amorphous. The amorphous phase is beneficial due to its low deposition temperature and the preservation of relatively high electron mobility compared to the crystalline material. A field-effect mobility of 80 $cm^2/(V\ s)$[4] was obtained on monocrystalline channels of $InGaO_3(ZnO)_5$. Polycrystalline films of such a structure have a Hall mobility of 20 $cm^2/(V\ s)$,[55] while amorphous IGZO (a-IGZO) has a typical Hall mobility of 10−20 $cm^2/(V\ s)$.[6,7] The decrease of mobility for only less than a decade indicates the limited impact of randomization of atomic configuration on the electron transport compared to other semiconductors, like Si and Ge. On the other hand, the onset of chemical reduction happens at a lower energy for a-IGZO. The random nature of a-IGZO causes a distribution of oxygen bond strengths, resulting in easier removal of some oxygen.[8] Since the free electron density is related to oxygen vacancies,[9−11] a-IGZO is less electrically stable. Therefore, the crystalline structure draws a lot of attention in improving the stability and also in understanding the properties of the amorphous phase. The IGZO crystal is a relevant starting model to simulate the electrical behavior of a-IGZO.[12]

The default crystal topology of IGZO belongs to the hexagonal family and exists in two polytypes, represented by the space groups $R\bar{3}m$ (160) and $P6_3/mmc$ (194). The structure of both polytypes consists of similar planes of In^{3+} cations, forming InO_2 sheets that laminate separated $Ga_xZn_yO_{(x+y)}$ layers.[13,14] The relatively high mobility in the amorphous phase is related to the isotropic spread of $5s^0$ orbitals, especially the ones related to In.[15] Enlarged orbital overlaps increase the delocalization of states at the bottom of the conduction band.[12,16,17] Therefore, electron mobility increases with increasing In concentration[18] and is independent of the directional arrangement of the metal cations, preserving the mobility in a-IGZO. Still, crystalline IGZO

Received: December 23, 2021
Accepted: February 13, 2022
Published: February 23, 2022

https://doi.org/10.1021/acsaelm.1c01315
ACS Appl. Electron. Mater. 2022, 4, 1238−1249

shows different electrical properties like improved thermoelectric performance,[19,20] confinement of holes,[21] and enhancement of electrons conduction paths,[12,22] resulting in anisotropic mobility as is observed on grown monocrystals.[23] Those effects are all related to the layered arrangement of InO_2 segments, where the orbital overlap is maximal. The layered crystal structure is also characteristic for an intermediate phase between amorphous and crystalline IGZO, maintaining a periodic lattice configuration along the *c*-axis only, while remaining structureless along the *a*- and *b*-axes.[24] Modeling anomalous X-ray scattering showed a preserved middle range order originating from the InO_x planes aligned parallel to $GaZnO_y$ slabs.[25,26] The remaining periodicity along the *c*-axis resembles the hexagonal structure of monocrystalline IGZO. The preferential orientation of the crystals in this film (texture) is with the alignment of the *c*-axis perpendicular to the substrate. This *c*-axis-aligned crystalline (CAAC) phase can be deposited with physical vapor deposition (PVD)[27] at deposition temperatures (T_d) around 300 °C,[28] which is remarkably lower than the crystallization temperature a-IGZO ($T_d \sim 600$ °C[7,29,30]). CAAC-IGZO is less sensitive for defect formation,[31] resulting in improved performance and better reliability.[32] Similar properties are also assigned to nanocrystalline (nc-)IGZO, another intermediate semicrystalline morphology without clear grain boundaries.[33]

With hexagonal (poly)crystalline, nc-, CAAC-, and a-IGZO, the morphology of the IGZO family is not complete. In this work, we show the formation of polycrystalline IGZO with a spinel polytype, represented by space group $Fd\bar{3}m$ (227). We refer to this material as "spinel IGZO" to distinguish it from hexagonal polycrystalline IGZO ("pc-IGZO"). Spinel IGZO can be obtained by PVD, using intermediating process conditions compared to a- and CAAC-IGZO. Pure spinel IGZO (free of CAAC and amorphous phase) is achieved using a template layer of spinel Ga_2ZnO_4 (GZO). In this way, the electrical performance of spinel IGZO is demonstrated in thin-film transistors (TFTs). With density functional theory (DFT) calculations, we finally compare the stability of the spinel to the CAAC phase and estimate the potential benefit in electrical performance

EXPERIMENTAL SECTION

IGZO films are deposited on thermally oxidized 12-in. (100) Si wafers using reactive sputtering with an Ar/O_2 gas mixture on a polycrystalline $InGaZnO_4$ target (In/Ga/Zn = 1:1:1, JX Nippon) in an Applied Materials Impulse chamber, installed on an Applied Materials Endura platform with vacuum load-locks. A degas chamber is used to remove moisture from at 350 °C in Ar ambient at 3−10 Torr. After degassing, the wafers pass a cooling station and enter the PVD chamber. A resistively heated wafer chuck with electrostatic clamping was used to vary T_d between 25 and 375 °C. PVD was performed in an Ar/O_2 mixture for which the O_2%-flow ratio (R_{O_2}) ranged between 10 and 90% at 2−5 mTorr pressure. Exploration of the process window was performed in a similar approach as was done by Cornell University[34] but with a different electric power supply to the target. Instead of radio frequency (RF) discharge, a magnetron pulsed DC setup was used. The pulse frequency was set between 50 and 200 kHz with a duty cycle of 5−40%, keeping the total sputtering power between 200 and 500 W.

Film composition was measured by wavelength-dispersive X-ray fluorescence spectroscopy (XRF) using a Malvern Panalytical 2830ZT Wafer Analyzer, equipped with a Rh X-ray source, set at 32 kV and 125 mA. The fluorescent channels of Zn Kα, Ga Kα, In Lα, and O Kα are carefully calibrated by X-ray photoemission spectroscopy (XPS), Rutherford back-scattering (RBS), and energy-dispersive X-ray (EDX) spectroscopy, executed in a transmission electron microscope (TEM) using a Titan^3 G2 60-300 (FEI). The resulting atomic ratio of In/Ga/Zn is 38:36:26%, for 200 nm a thick IGZO film (R_{O_2} = 90%, T_d = 200 °C). The absolute accuracy, estimated from the systematic errors of XPS and XRF, is within ±2%. The oxygen atomic concentration of IGZO was 57 ± 1%, showing a stoichiometric composition matching the stoichiometry of the binary oxides. The composition of films, with a thickness of 50 nm or less with different R_{O_2} and T_d are monitored by XRF showing the average composition to be slightly In-rich and Ga-poor with In/Ga/Zn = 39.7:34.0:26.3%, all within an absolute variation of ±2% except for films at R_{O_2} = 0% (33.9:31.4:24.3%) or T_d = 300 °C (40.4:35.3:24.3%) (see Figure S.1, Supporting Information).

X-ray diffraction (XRD) is performed on a Jordan Valley JVX tool using a Cu Kα source set at a grazing incidence (GI) angle of ω = 1° for ω−2Θ measurements (GI-XRD) or using an out-of-plane or Θ−2Θ measurement with a 1° sample tilt. To determine the texture of the film, the incident beam and detector are fixed to the characteristic diffraction angle 2Θ_c, while ω is varied by tilting the wafer (Θ−ω XRD). Si wafers were always rotated with ϕ = 22° to orient the Si[001] away from the plane of the X-ray beam path to avoid detection of residual diffractive scattering in Si substrate. To explore phase changes during thermal annealing above T_d, in situ XRD (IS-XRD) is performed in an in-house built heating chamber, integrated into a Bruker D8 Discover diffractometer using a Vantec linear detector covering a 2Θ range of 20° and a fixed ω = 15°. XRD patterns for 2Θ = 20−40° are collected every 5 s during heating the sample at a rate of 0.2 °C/s from room temperature to 900 °C in an inert He atmosphere. The onset of crystallization of a-IGZO was observed to occur above ca. 650 °C. For a systematic and detailed comparison of crystallized IGZO, annealing was done at 700 °C in an atmospheric batch furnace system in 1 atm O_2 ambient for 1 h.

MORPHOLOGY

The best condition to deposit CAAC-IGZO is $T_d \sim 300$ °C and R_{O_2} = 20−90%.[34] Figure 1 shows the evolution of the GI-XRD spectrum of 50 nm thick IGZO films with increasing T_d for R_{O_2} = 90%. At T_d = 25 °C, the spectrum shows the typical signature of a-IGZO: broad diffraction bands around 2Θ = 32 and 56°.[28,34,35] When T_d = 300 °C, the band at 56° is

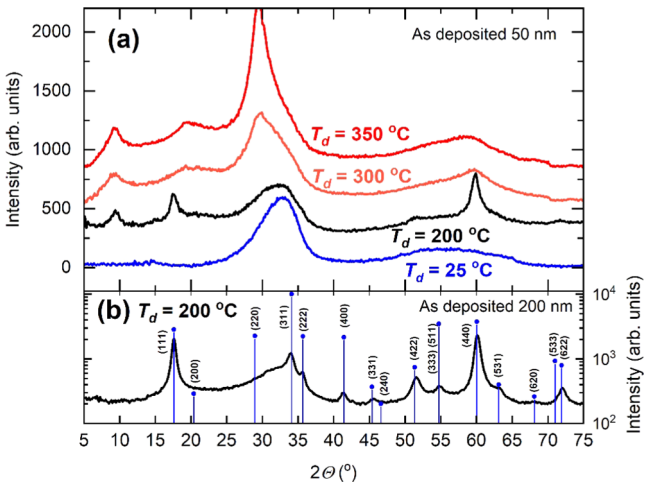

Figure 1. GI-XRD spectra of 50 nm obtained for different T_d values (a). At T_d = 200 °C, two peaks are formed at 17.8 and 60° and are an indication for the formation of spinel IGZO. For 200 nm thick films, other spectral details appear (b) and are matching with the simulated diffraction peaks for spinel IGZO with a lattice constant of 8.676 ± 0.11 Å, indicated by the blue vertical lines.

https://doi.org/10.1021/acsaelm.1c01315
ACS Appl. Electron. Mater. 2022, 4, 1238−1249

diminished, while at 32°, a broad asymmetric peak emerges, shifting down to 30° at a higher temperature. This peak is related to the formation of CAAC[25] and is often attributed to diffraction to (009) planes, which is the most dominant in the hexagonal structure of $InGaZnO_4$. Also, the diffractions on (003) and (006) planes at respectively 10.1 and 20.4° are visible. Remarkably, before the onset of CAAC formation at around $T_d \sim 200$ °C, the spectrum is different with the appearance of two peaks, one at $2\Theta = 17.8°$ and another at 60.1°. With increasing thickness, other lower-intensity peaks appear in the GI-XRD spectrum.

The out-of-plane XRD spectrum differs from GI-XRD. Weak diffraction of a-IGZO is suppressed by the limited path length of X-rays through the material, so the broad band at 32° is limited. The perpendicular alignment of the *c*-axis planes to the substrate surface enhances the diffraction of CAAC-IGZO and the dominant (009) diffraction is visible as a clear signature of this phase. Next to the two peaks, a third peak appears at $2\Theta = 35.5°$ with a maximum at around $T_d = 200$ °C (Figure 2). This peak is still present as a shoulder in the CAAC diffraction at $T_d = 300$ °C. In GI-XRD, this peak is only visible in thick IGZO films.

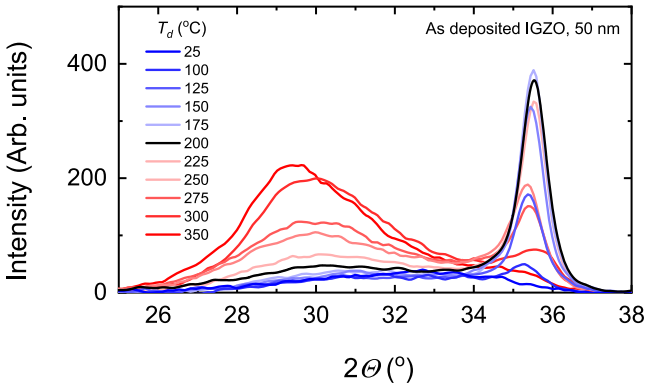

Figure 2. Θ−2Θ XRD spectra for 50 nm thick IGZO deposited at different T_d values, at 500 W and 90% R_{O_2}. The broad peak at around $2\Theta = 30°$ is assigned to the formation of CAAC-IGZO. The sharper peak at 35.5° is the (222) diffraction of spinel IGZO, which has a maximum intensity at $T_d = 200$ °C and is indicated by the black line.

The three new peaks, most dominating at $T_d = 200$ °C, were previously linked to the presence of spinel IGZO, formed after laser annealing of amorphous films.[36] The peaks at 17.8 and 35.5° can be assigned to the diffraction from {111} and {222} planes. An Θ−ω XRD scan (inset of Figure 3) shows the alignment of the {111} and {222} planes to be within ±8° parallel to the substrate surface, indicating a texture, identical to CAAC-IGZO.[34] The peak at 60.1° is related to diffraction to the {440} planes, which have an angle of 35.3° to ⟨111⟩ directions. The ±8° alignment variation in the texture brings the diffraction of the {440} and {111} planes in the observation range of GI-XRD configuration, but only in out-of-plane XRD, all higher diffractions of the [111] direction are observable (see Figure 3). With increasing thickness, the film loses texture, which, together with the enlargement of scattering volume, makes the whole diffraction spectrum of the spinel phase visible in GI-XRD (Figure 1). Now, also (311)- and weaker diffractions are detected, confirming the existence of spinel IGZO with a lattice constant of 8.676 ± 0.11 Å. Grain sizes are calculated from the peak half-width at

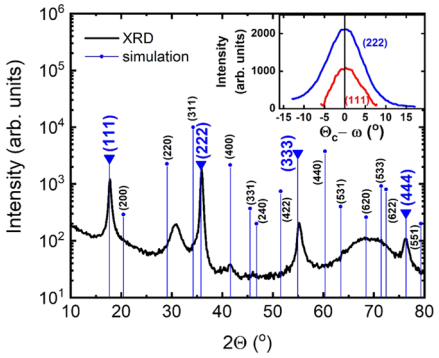

Figure 3. Out-of-plane XRD of a 200 nm thick IGZO film deposited at 200 °C and the theoretical diffractions for spinel IGZO. For this measurement, the wafer was tilted at 4° to suppress the Si(100) diffraction at 70°, which still causes an increased background in this spectrum. The preferential texture in the [111] direction provides only the observation of (111) and higher-order peaks as indicated by the blue triangles. In the inset, the peak intensity of (111) and (222) diffraction is given for tilting the sample.

full maximum with the Scherrer equation and are in the range of 10−12 nm for 50 nm thick films.

The spinel polycrystals are smaller and blended with the amorphous or CAAC phase in the first 20−50 nm of the film. The amorphous or CAAC phase is formed at the start of deposition and gradually transforms into the spinel phase. Both the starting phase and the gradient of phase mixture are depending on the O_2-flow ratio, DC power, and T_d. At $T_d = 200$ °C, most spinel phase is found for the highest O_2-flow ratio (90%) and the highest power (500 W) (see Figure S.2, Supporting Information). To observe the presence of amorphous IGZO in XRD, annealing at 700 °C in O_2 ambient for 1 h can be used to crystallize the film. Films at $T_d = 25$ °C are amorphous and crystallize during annealing into pc-IGZO. The main diffractions of this hexagonal phase are at the (009) and (101) planes and their closely neighboring position at $2\Theta = 30.8$ and 31.47° are merging into a broad peak at 31.3° (see Figure 4). The diffraction at (003) and (006) planes and other lower diffractions are also becoming visible due to crystallization.[29,30] In the case of $T_d \geq 300$ °C, the broad diffraction band of CAAC around 30° narrows and shifts slightly to 30.5°. This shift is attributed to the further crystallization of CAAC in which the *c*-axis alignment loses alignment to the substrate surface as can be observed by the increase of the other CAAC-related diffractions at (003) and (006) planes, while other smaller diffractions related to pc-IGZO remain absent. This phase is referred to as "poly-CAAC" to distinguish it from the pc-IGZO and the surface-aligned CAAC. For the $T_d = 200$ °C, at which spinel IGZO is formed, 700 °C annealing causes crystallization of the present CAAC/a-IGZO but did not change the peaks related to spinel IGZO.

Annealing at 700 °C is a useful process step to identify the presence of a-IGZO and to determine the purity of the other phases like CAAC and spinel IGZO for different process conditions. In Figure 5, the spectrum of out-of-plane XRD of the same 50 nm thick IGZO films as in Figure 2 are shown, but now after 700 °C annealing. Both the hexagonal and poly-CAAC phases are identified by their distinct peaks at, respectively, 31.3 and 30.5°. For the films $T_d = 25-200$ °C, the hexagonal peak is systematically lowered with increasing T_d and shifts to lower 2Θ. This shift continues with increasing T_d beyond 200 °C, but the amplitude systematically increases

https://doi.org/10.1021/acsaelm.1c01315
ACS Appl. Electron. Mater. 2022, 4, 1238−1249

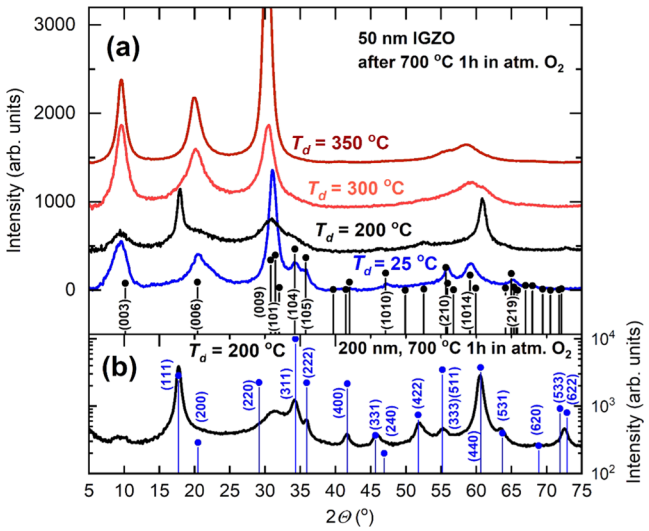

Figure 4. GI-XRD spectra of 50 nm obtained after 700 °C 1 h O_2 anneal for different T_d values (a). For $T_d \geq 300$ °C, the CAAC is crystallized into poly-CAAC. At $T_d = 25$ °C, the initial amorphous film crystallizes into pc-IGZO and can be distinguished from the features in the spectra that correspond to the simulated diffractions (black dots) for hexagonal IGZO. At $T_d = 200$ °C, the spectrum is hardly changed from Figure 1. Films of 200 nm (b) still show similar details corresponding to the simulated diffraction of spinel IGZO (blue dots).

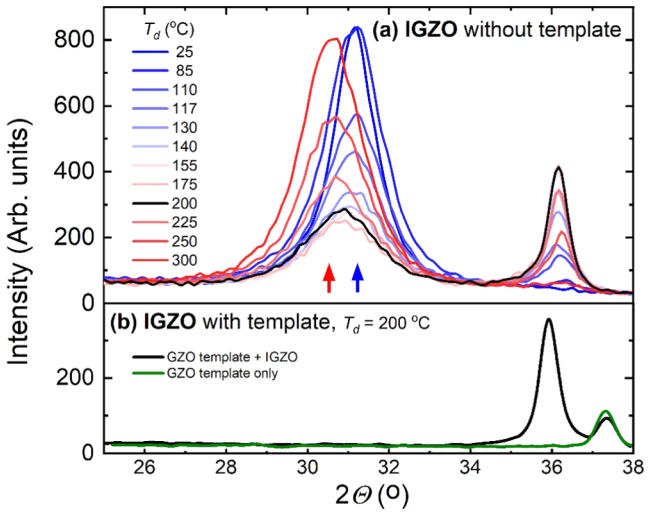

Figure 5. (a) Θ−2Θ XRD spectra after 700 °C O_2 annealing of 50 nm thick IGZO deposited at different T_d values, 500 W, and 90% R_{O_2}. The broad peak at 2Θ = 30.8° is assigned to pc-IGZO, crystallized from a-IGZO that is mainly formed at low T_d (blue curves). For a high T_d, the peak shifts to 31.3° due to the formation of poly-CAAC (red curves). At a medium T_d (around 200 °C, black line), the amount of pc-IGZO and poly-CAAC is lowest, while the spinel phase is at maximum as witnessed by a maximum peak intensity of the (222) diffraction at 35.5°. (b) IGZO (24 nm thick) after 700 °C O_2 annealing on a 10 nm spinel GZO template. No (poly-)CAAC- or pc-IGZO is observed, demonstrating the absence of a- and CAAC-IGZO.

again, showing a complete poly-CAAC phase at 300 °C. At 200 °C, the presence of the hexagonal and poly-CAAC is minimal and both peaks are merged. At this temperature, the spinel phase, witnessed by the diffraction peak at 35.5°, is at its maximum intensity. Note that no change in shape or amplitude of this diffraction peak is observed after annealing, indicating that no additional spinel phase is formed during annealing. This stability of the spinel phase is also evidenced by in situ XRD, as shown in Figure 6. Up to 900 °C annealing, the (222)

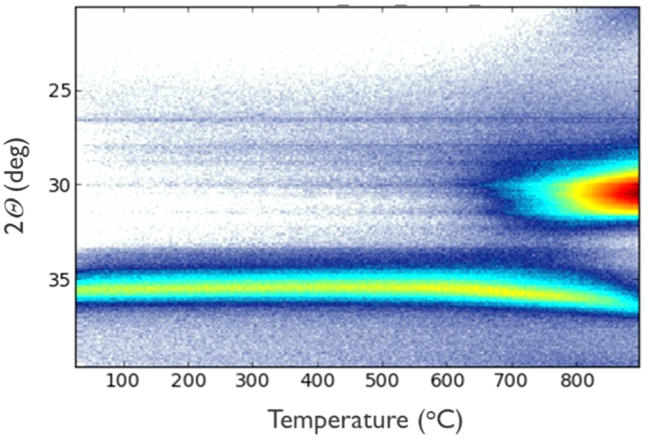

Figure 6. In situ XRD $\omega = 15°$. XRD patterns for 2Θ = 20−40° on 50 nm IGZO in He atmosphere. Crystallization of the amorphous bottom layer starts at ∼650 °C, while the spinel phase remains intact up to 900 °C.

diffraction at 35.5° remains stable, while a broad peak centered at 30.5° starts to appear above ∼650 °C, with a maximum at the end of the annealing range at 900 °C. The annealing tests also demonstrate phase stability of spinel IGZO above 700 °C, a temperature at which a-IGZO crystallizes into pc-IGZO and causes a collapse of carrier mobility.[30,37]

We conclude that spinel IGZO is a metastable phase formed between the intermediate deposition conditions of amorphous and CAAC. Deposition at $T_d = 200$ °C does not cause the direct formation of clearly defined spinel crystallites, but rather a proto crystalline film is formed first. This proto crystalline spinel phase is present in the first ∼20 nm. The electrical properties of this proto crystalline film were earlier investigated by Glushkova et al.[38] To study the properties of pure spinel IGZO, the presence of the proto crystalline interface needs to be avoided. This can be done by stimulating the formation of spinel IGZO directly at the start of the deposition using a crystal template. Crystalline Ga_2ZnO_4 (GZO) cannot have the hexagonal structure of pc-IGZO because it lacks indium. Instead, crystallization happens only into the spinel form and can therefore easily be obtained. Both atomic layer deposition (ALD) and combinatorial sputtering can be used to obtain a-GZO from the co-deposition of Ga_2O_3 and ZnO. Annealing for 1 h in O_2 ambient at 700 °C crystallizes the film into the spinel phase. When IGZO is deposited on top of GZO, the phase is also spinel. The lattice spacing of spinel IGZO is 4% larger compared to GZO. This difference is clearly observed with GI-XRD, as shown in Figure 7d. Due to the texture, (111), (311), (422), and (440) are aligned sufficiently to the grazing angle geometry to cause diffraction. But now, double peaks appear because of the different lattice spacing between IGZO and GZO. Despite this lattice mismatch, spinel IGZO grows readily on the GZO template, preserving its texture.

The transmission electron micrograph (TEM) image in Figure 7 shows the templating effect by the continuous propagation of the crystal orientation from the GZO into IGZO. No distinguishable interruption can be seen at the interface. Fast Fourier transform images on areas above and below the interface show electron diffraction in similar

https://doi.org/10.1021/acsaelm.1c01315
ACS Appl. Electron. Mater. 2022, 4, 1238−1249

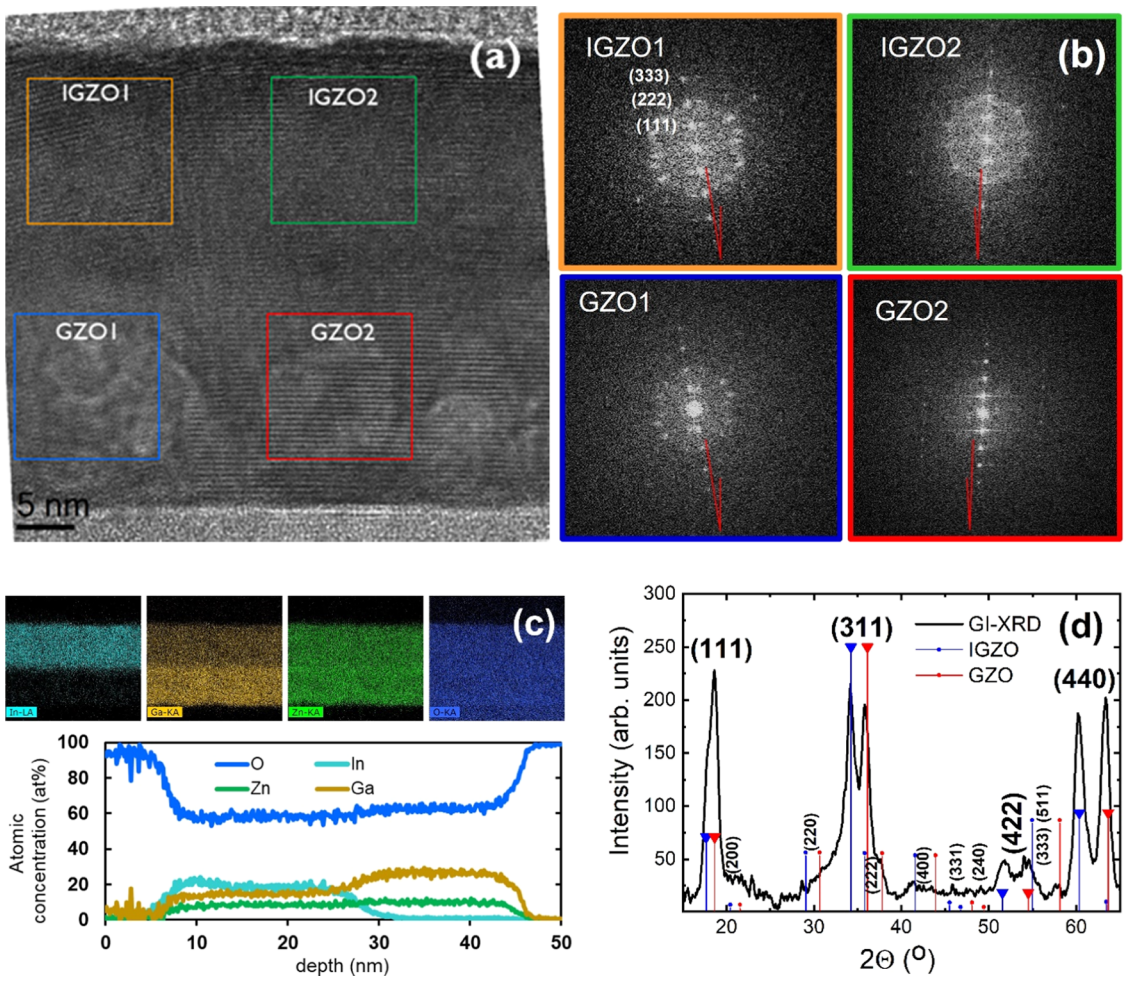

Figure 7. (a) Cross section of 18 nm spinel GZO with 20 nm IGZO (T_d = 200 °C) on top. (b) Fast Fourier transform images of the scans in the indicated areas showing the crystalline orientation of IGZO to be the same as the GZO beneath. The [111]-direction, related to the surface normal, is identified by (111)-diffraction spots and is indicated by a red line. (c) EDX cross-sectional maps and line scans of the elemental composition of the GZO/IGZO stack. (d) GI-XRD scan of the GZO/IGZO, showing double peaks originating from similar diffraction planes but different plane spacings between GZO and IGZO.

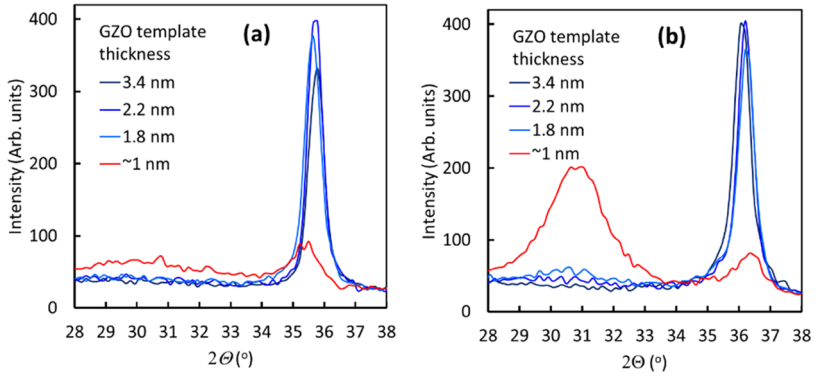

Figure 8. (a) Θ−2Θ XRD spectra of 24 nm thick IGZO deposited at different T_d values, 500 W, and 90% R_{O_2} on spinel GZO templates with thicknesses of ca. 1−3.4 nm. The sharp diffraction peak at 35.5° shows the spinel phase of IGZO. Deposition of spinel IGZO is achieved for templates as thick as 1.8 nm. For ∼1.0 nm, the IGZO is mainly amorphous. (b) Same, but after 700 °C O_2 annealing. No additional crystallization is observed, except for the lowest template thickness (∼1 nm), the a-IGZO crystallizes into pc-IGZO, indicating the failure of templating.

orientation, demonstrating the templating effect. Most diffraction patterns (Figure 7b) reveal a periodicity oriented close to the normal of the surface, with the main lattice spacings (d) in the IGZO film d = 2.557 and 5.117 Å, matching (222)- resp. (111)-planes, while slightly smaller lattice spacings are observed for the GZO template below. No amorphous IGZO could be observed at the interface, despite a small gradient of In and Ga in the EDX analysis (Figure 7c). The absence of a-IGZO is further evidenced by submitting the samples to a second O_2 annealing at 700 °C, after the

https://doi.org/10.1021/acsaelm.1c01315
ACS Appl. Electron. Mater. 2022, 4, 1238−1249

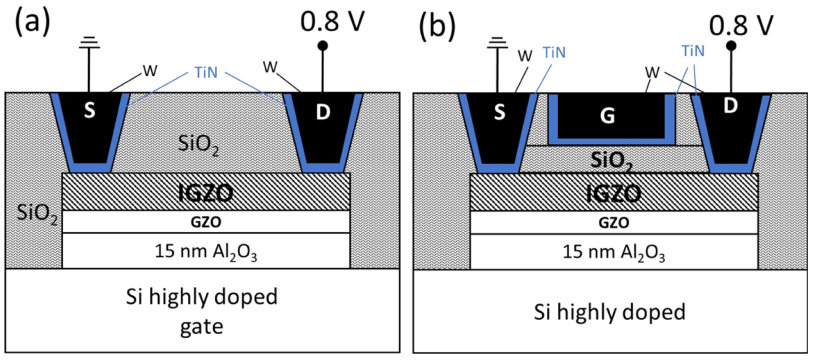

Figure 9. (a) Schematic layout of back-gated IGZO devices and (b) front-gated devices.

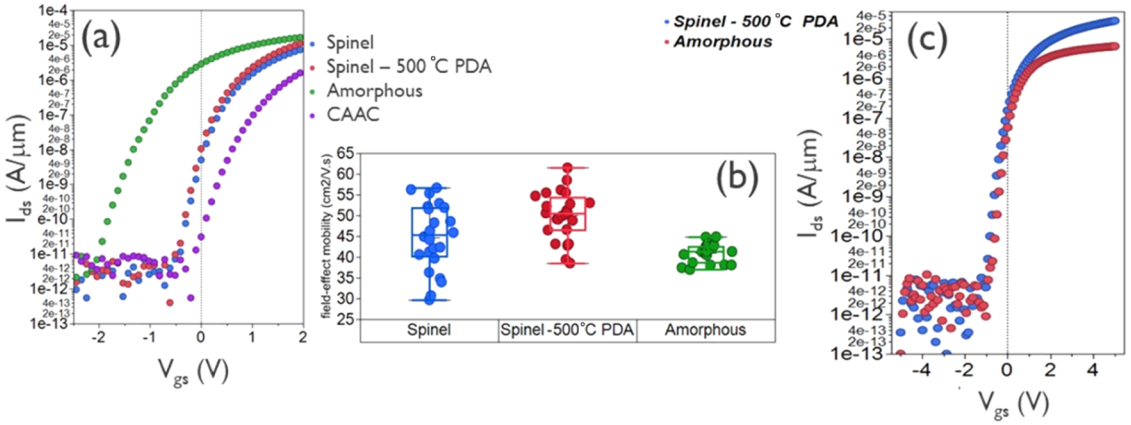

Figure 10. (a) I_{ds} of back-gated devices with W = 1 μm and L_g = 135 nm for different IGZO types with a thickness of 10 nm. The back-gate configuration is as given in Figure 9a. (b) Corresponding field-effect mobilities derived from L_g = 10 μm to eliminate source−drain contact resistance. (c) I_{ds} of back-gated devices with scaled dimensions (L_g = 45 nm) for amorphous and spinel IGZO in the front-gate configuration as given in Figure 9b. For the back-gated test on the FG config structure, the real L_g is defined by the top gate L_g plus 2 times the distance between the contact to the gate (15 nm). Therefore, the real L_g is 75 nm.

deposition of IGZO. No XRD signature of pc-IGZO or an increase of spinel IGZO has been observed as shown in Figure 5b. Only the (222) peak at 37.3° of the spinel GZO template is now visible, next to the one of IGZO. The spinel GZO template can be thinned down to 1.8 nm while preserving its templating effect (Figure 8). Only at 1 nm, pc-IGZO appears after annealing. At this thickness, the template is too thin to enable an appropriate crystallization in the first annealing. The lack of a templating effect causes the formation of amorphous IGZO at the interface as can be witnessed by crystallization into pc-IGZO after annealing. Apart from the templating effect, the window of PVD conditions in which spinel IGZO is obtained is increased to the wide range of T_d = 25−250 °C.

■ ELECTRICAL PERFORMANCE

To demonstrate the electrical functionality of pure spinel IGZO, we tested the material in scaled back-gated TFTs. The layout of the IGZO FET device is provided in Figure 9a. On top of 15 nm Al_2O_3, a template of spinel GZO with a thickness of 2 or 6 nm thickness is formed. Next, 10 nm IGZO is added at T_d = 25 °C and 200 °C, R_{O_2} = 90% for spinel; T_d = 300 °C, R_{O_2} = 0% for a-IGZ;O and T_d = 300 °C, R_{O_2} = 90% for CAAC-IGZO. Subsequentially, the IGZO is covered with 10 nm SiO_2 low-temperature plasma-enhanced chemical vapor deposition (PECVD) as a gate dielectric. The active area is then patterned down to the Si substrate. Source/drain (S/D) contact trenches are opened through a SiO_2 field oxide, where TiN and W are deposited, respectively, by PVD and ALD/CVD. The highly doped Si substrate under the Al_2O_3 layer acts as the bottom gate. To provide electrical access to the smallest devices, additional metallization layers are implemented via subsequent patterning steps. To reduce the oxygen vacancies, an O_2 annealing at 350 °C is applied after the last metallization step. During the electrical tests, a voltage sweep is applied to the Si substrate and the drain voltage is set to 0.8 V.

The drain current is modulated by sweeping the gate potential bias (V_{gs}) in the positive direction and depends on the electron concentration in the channel. In Figure 10a, the source−drain current (I_{ds}) vs V_{gs} is shown for transistors with a comparable threshold voltage (V_t) but different morphology of the IGZO channels. Because the band gap of GZO is ∼4.5 eV,[39] significantly larger than spinel IGZO ∼3.2 eV, the channel conduction in TFT is confined to the IGZO layer. The GZO template functions as an insulator since no I_{ds} can be detected in TFTs consisting of the GZO template only (not shown). With the GZO template present, all IGZO channels are performing well, except for CAAC. The I_{ds}−V_{gs} curves are obtained for devices with channel width W = 1 μm and length L_g = 135 nm and show comparable characteristics, with I_{on}/I_{off} > 10^5. While the a-IGZO channel shows V_t < −1 V, crystalline channels lead to a much higher V_t. However, the CAAC phase shows a strong degradation of I_{on}. Therefore, the spinel phase enables an optimum trade-off between V_t and I_{on}. The figure also shows the transfer characteristics of an IGZO TFT where

https://doi.org/10.1021/acsaelm.1c01315
ACS Appl. Electron. Mater. 2022, 4, 1238−1249

the spinel channel underwent postdeposition annealing (PDA) at 500 °C, indicating that a slightly higher I_{on} can be achieved with this additional step. This result is confirmed by the field-effect mobility (μ_{FE}) extracted from $I_{ds}-V_{gs}$ curves from devices at L_g = 10 μm. In Figure 10b, the μ_{FE} extracted for 23 devices, uniformly distributed over the 300 mm wafer are shown for spinel and a-IGZO. Spinel IGZO ensures higher mobility than amorphous IGZO, and the 500 °C PDA further improves the performance, reaching a median mobility of 50 $cm^2/(V\ s)$.

To further explore the performance of spinel IGZO devices and their potential use for stacking-compatible capacitor-less DRAM cells with >400 s retention time,[40] a similar device structure was built in a front-gated configuration (Figure 9b). Now a 7 nm SiO_2 serves as a front gate dielectric, with a TiN/W stack acting as gate metal terminal. The wafers underwent multiple annealing cycles in O_2 to achieve the highest possible V_t. Figure 10c shows the transfer characteristics collected for spinel and amorphous IGZO on scaled transistors with W = 1 μm and L_g = 45 nm (real L_g = 75 nm, see Figure 10c), clearly revealing that the spinel phase enables a higher I_{on} for a similar V_t.

DFT SIMULATIONS

Having demonstrated the existence and electrical functionality of stoichiometric spinel IGZO, two fundamental questions remain to be answered to establish if it has the potential for being a better channel material than a-IGZO or even hexagonal IGZO. The first one is: where does spinel IGZO rank in stability compared to the other phases? Spinel IGZO has not been reported as deposited films for such a high indium atomic percentage,[41] still spinel IGZO can be obtained from PVD using In/Ga/Zn = 1:1:1 targets. Second, what is the potential ultimate gain in device performance? Both questions can be theoretically approached by simulations on the spinel IGZO structure, comparing it to models for CAAC- and a-IGZO. By calculating the configuration energy, the relative stability can be obtained, and from the effective electron mass (m^*), a crude first-order evaluation of the electron mobility can be made.

We have performed first-principles calculations using density functional theory (DFT).[42−44] In all calculations, we use the PBEsol generalized gradient approximation for the exchange-correlation functional.[45,46] All computational details are provided in the Supporting Information. We first optimize the structure and calculate its total energy using CP2K.[47] In this way, we can compare correctly to previous work on crystalline and a-IGZO phases. Next, we study in detail the electronic structure using the Abinit software package[48−50] using norm-conserving pseudopotentials from the PseudoDojo[51] and analyze the results using the AbiPy package. The crystal structure of spinel IGZO is based on that of spinel GZO but with half the Ga atoms in the octahedral sites replaced by In. Since Ga sites and In sites cannot be distinguished easily by XRD and the elements are rather similar chemically, we investigate the In−Ga disorder explicitly. The primitive unit cell of spinel GZO, in space group $Fd\bar{3}m$ (227), contains two formula units (f.u.) of $InGaZnO_4$. To allow for a bit more freedom and a larger span of In/Ga ratios we work in a twice as large cell for spinel IGZO. In total, the In and Ga atoms can be distributed over the octahedral sites in this cell in seven symmetry-inequivalent ways. We construct all of these seven options and compare their properties. Due to the partial replacement of Ga by In, the symmetry is broken and representation has to be reduced to space group $P222_1$ (17). Positions of the other six possible configurations are given as CIF files in the Supporting Information. The most stable configuration of In and Ga atoms for In/Ga = 1:1 in the 4 f.u. cell of spinel GZO is shown in Figure 11. This reference

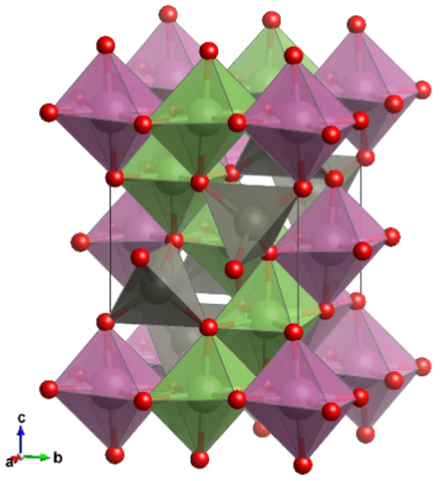

Figure 11. Reference configuration of spinel IGZO with In/Ga = 1:1, represented in the space group $P222_1$ (17) to allow a lower symmetry by alternating occupation of octahedrally coordinated sites by In (pink) and Ga (green). Tetrahedrally coordinated sites are always occupied by Zn (gray).

configuration is only 0.016 eV/f.u. less stable than a perfectly crystalline model of hexagonal IGZO, with In/Ga/Zn = 1:1:1, represented by space group $Fd\bar{3}m$ (227), which is here considered as a model for CAAC-IGZO. For comparison, amorphous models tend to be 1.21 eV/f.u. less stable than CAAC-IGZO. The variation in total energies between the different In−Ga distributions is in the order of 0.1 eV/f.u. (see Figure 12). At the PBEsol level, we calculate a band gap of 1.7 eV and a corresponding effective mass m^* = 0.2 m_0 for our most stable spinel structure. Note that generally DFT predicts

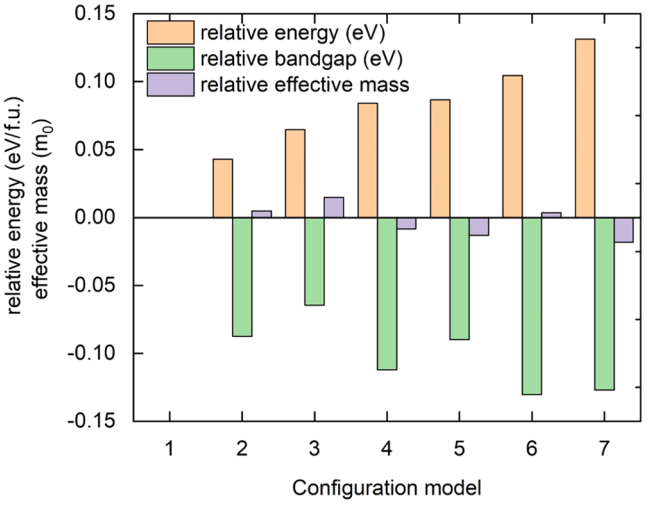

Figure 12. Total energy, band gap, and effective electron mass (m^*) for spinel IGZO with In/Ga/Zn = 1:1:1 with different In and Ga configurations compared to the reference configuration given in Figure 11.

https://doi.org/10.1021/acsaelm.1c01315
ACS Appl. Electron. Mater. 2022, 4, 1238−1249

the true ground-state electron energy but not the excited states. Therefore, the calculated band gap is underestimated and can only be used for relative comparison. The band gap of our perfectly crystalline model is 1.2 eV with m^* = 0.25 m_0. Experimentally reported m^* for amorphous IGZO are in the order of 0.30−0.37 m_0.[16] We stress here that the effective masses for our crystalline solids are calculated as band effective masses from the curvature of the bottom conduction band at Γ. For amorphous materials, this concept is not valid since the lacking periodicity renders the Bloch theorem inapplicable making the notion of a band structure invalid. The notion of an effective mass remains, but it is not related to a curvature of bands anymore. The band structures of all models are provided in the Supporting Information (Figure S.3). Figure 12 also visualizes the distribution of the band gap and the effective mass. The values are shown relative to the reference configuration, the most stable distribution of In and Ga atoms for In/Ga = 1:1. We observe an overall inverse relationship between the total energy of the structure and its band gap, but the effective masses do not follow this trend clearly. Most important to note is that the variations in the gap and effective mass are rather limited. The band gap changes maximally 9% from the value of the most stable structure and the effective mass 7%. We hence conclude from the small variations in total energies that a certain amount of In−Ga disorder is to be expected in spinel IGZO, but that electronically this does not have significant consequences.

Finally, we also construct all symmetry-inequivalent options for distributing the In and Ga atoms in nonstoichiometric ways and we derive the average lattice constants for the unit cell by projecting the dimensions of all symmetry-inequivalent distributions of In and Ga. Lattice constants for the *a*-, *b*-, and *c*-axes are shown in Figure 13. Variations between the

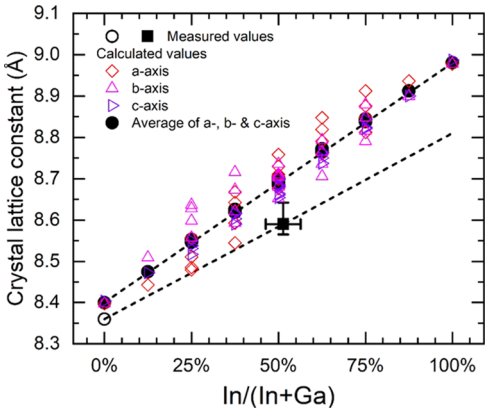

Figure 13. Calculated lattice constants of the cubic $Fd\bar{3}m$ unit cell for different In/Ga ratios in spinel IGZO. The open triangles are the lattice constants of the *a*-, *b*-, and *c*-axes for different In/Ga configurations and are averaged (black dots). The open circle at 0% In/(In + Ga) is the literature value for spinel GZO, the closed black square is the value for spinel IGZO obtained in this work.

lattice constants are caused by the three possible orientations of each distribution that appear to be repeated throughout the crystal material because of the periodic boundary conditions in the DFT calculation. Averaging the lattice constants for each axis removes this artifact and provides a single lattice constant for a symmetric cubic $Fd\bar{3}m$ unit cell, representing the lattice constant for spinel IGZO with a random distribution of In and Ga for each In/Ga ratio. The average values show a clear linear trend, following Vegard's law: i.e., for a fixed crystal structure containing two constituents, the lattice parameter is the weighted mean of the lattice parameter of the two individual constituents. Our experimental values are presented by a black dot in Figure 13. The vertical error bar for the lattice constant is obtained from the observed variations of the (222) diffractions in XRD. The horizontal error bar is the minimal and maximal In/(In + Ga) ratio of cations in the octahedral positions, derived from the composition measurements. Here, we assumed that a maximal amount of Ga, resp. In atoms is in the tetrahedral position due to the Zn deficiency, giving In/(In + Ga) = 0.47, resp. 0.57. In case the cation positions are not contributing to changes in the crystal dimensions, this error bar is smaller: 0.49−0.54. From this experimental value, we can extrapolate a linear trend from GZO (8.36 Å) to the hypothetical value for In_2ZnO_4 (8.81 Å). The calculated trend has a systematic larger lattice constant and the offset is increasing with increasing indium concentration. The calculated lattice constants depend on the used exchange-correlation functional,[52] and its correction can be estimated by comparing calculated lattice constants to known real values. The calculated lattice constant for bixbyite In_2O_3 (10.299 Å) has an offset of 0.18 Å compared to the experimental value (10.117 Å[53]). This offset is larger than the offsets of 0.07 and 0.04 Å for the experimental values of spinel GZO based on the literature (8.334 Å[54]), resp. our observation but close to the offset with our hypothetical value for In_2ZnO_4 (0.17 Å). Using this correction validates the assumption that the experimental difference of XRD diffraction peaks between GZO and IGZO is induced by an increase of lattice constant due to the indium atoms, replacing ∼50% of the gallium.

DISCUSSION

The existence of crystalline spinel phases was previously reported in high-temperature metallurgical studies of IGZO.[14] GZO has a default crystalline phase in the spinel configuration, a cubic $Fd\bar{3}m$ unit cell with a distorted face-centered cubic oxygen lattice in which Zn takes tetrahedrally coordinated interstitial sites and Ga takes the octahedrally coordinated interstitial sites. The Ga atoms can be replaced gradually with In up to 6.4%.[41] This corresponds to only 4.2% of all metal atoms. For higher indium concentrations, spinel IGZO is expected to be unstable and phases will segregate. For this reason, spinel In_2ZnO_4 was never reported to exist. The fact that pc-IGZO is always formed when crystallizing a-IGZO and no crystallization into spinel IGZO was detected shows that spinel IGZO with In/Ga = ∼1:1 is metastable to at least 700 °C. The disappearance of the (222) diffraction in IS-XRD (Figure 6) at 900 °C witnesses a high thermal stability of this phase, which is likely depending on the In concentration. Note that all films do have a composition deviating from the stoichiometry for spinel: (In + Ga)/Zn = 2:1. Films that do show a spinel signature have In/Ga/Zn = 39.7:34.0:26.3% or (In + Ga)/Zn = 2.8:1. This is in line with reported Zn deficiencies of films obtained by sputtering[55] and implicates that 10% of the In and Ga cations are populating tetrahedral sites, assuming a defect-free film. Occupation of a tetrahedral site by Ga is very well possible due to lowering of its oxidation state from 3+ to 2+. The polymorph of gallium oxide: γ-Ga_2O_3 is a cation-deficient spinel with partial occupancy of both tetrahedral and octahedral sites.[56,57] Occupation of a tetrahedral site by In or Ga is also possible when exchange happens with Zn cations as is the case in (partially) inverse

https://doi.org/10.1021/acsaelm.1c01315
ACS Appl. Electron. Mater. 2022, 4, 1238−1249

spinel.[58] However, our DFT simulations show an energetic cost of ~0.5 eV for exchanging In or Ga with Zn, which is confirmed by the fact that GZO is typically a normal spinel.[58] Therefore, we consider spinel IGZO to have a normal spinel structure in which octahedral sites are fully occupied by In and Ga. Small variation in total energy for different In and Ga configurations indicates no preferential occupation of the octahedral sites between In and Ga. Hence, In and Ga positions are fully randomized and following Vegard's law: the crystal lattice constant changes linearly with the In/Ga ratio and fits well with the theoretically calculated values. Ga and Zn cations are almost equal in size as is reflected by the small difference between spinel GZO (8.334 Å) and γ-Ga_2O_3 (8.238 Å), and therefore, the impact of Zn deficiency is assumed not to have much impact on the lattice constant.

No phase separation has been observed when spinel IGZO is annealed at 700 °C, but peak shifts at higher temperatures in IS-XRD indicate the onset of structural changes. When looking closely at the detailed position of the (222) spinel peak in the IS-XRD measurement, first, a decrease of ~0.2° can be seen, which can be explained by the thermal expansion of the crystal. At 700 °C, an increase up to 0.9° at 900 °C occurs, corresponding to a decrease of lattice constant with 0.2 Å. According to Vegard's law, this shrinkage of the lattice indicates a serious loss in indium from the spinel lattice structure, which could not be confirmed by composition measurements. Care must be taken with conclusions on local composition changes because local strain and crystal defects also induce deformation of the lattice. Also, relaxation in the spinel lattice by exchange between Zn and In or Ga in the occupation of octahedrally and tetrahedrally coordinates sites, as is observed in GZO,[39] must be taken into account. Moreover, crystal defects by the occupation of additional nonspinel sites will also contribute.[57] At least, the change of the XRD spectrum above 700 °C is an indication of structural changes in the spinel lattice that are related to the rearrangement of indium atoms. This is pointing toward the metastability of the spinel phase of IGZO, which is about to change into the CAAC phase well above the crystallization temperature of amorphous IGZO.

The formation of the CAAC phase is alternatively explained as a stress relief by separating into two different structures with different elastic moduli.[59] Remarkably, spinel IGZO has a large fraction of its crystals oriented in the [111]-direction, which has alternating levels of atomic arrangements in hexagonal shapes. InO_2 planes of hexagonal IGZO have similar in-plane structures. We calculated the formation energy of spinel IGZO to be very close to CAAC-IGZO, therefore spinel can be considered a metastable phase, losing its stability due to the presence of a large amount of indium. The formation of CAAC might happen by pushing indium out into InO_2 sheets, obtaining the arrangement of CAAC. We hypothesize that the spinel phase is an intermediate step into the formation of CAAC. Both spinel and CAAC phases are likely formed by the surface impact of ions rather than the formation from crystal-like clusters readily sputtered from the pc-IGZO target.[25] The crystallization is possibly induced by the impact of negative oxygen ions because the maximum diffraction intensity is observed at the highest R_{O_2} and a high power (see Figure S.2). Negative oxygen ions often provide an important contribution to crystallization during PVD[60] and are sufficiently available in the DC method.[61] The lack of energetic negative ions might be the reason why the deposition of IGZO in the spinel phase has not been reported for RF-PVD.[28,34] But when sufficient oxygen ions are provided, metastable spinel is formed at T_d = 200 °C. With increased T_d, the metastability of spinel causes a rearrangement into CAAC during deposition.

The existence of spinel IGZO raises the question of whether this phase is still metastable at an In/Ga ratio larger than 1:1. High indium concentrations in a-IGZO increase the electron mobility but decrease the stability of oxygen atoms, resulting in high free electron concentrations due to the formation of oxygen vacancies. This formation might be suppressed when IGZO is in the crystalline phase. Recently, the stability of oxygen in CAAC-IGZO, amorphous, and spinel IGZO (In/Ga/Zn = 1:1:1) was calculated and spinel IGZO appeared to be the most stable one.[8] However, phase separation into In_2O_3 and GZO is likely to occur for higher indium concentrations, but it will be interesting to know at which concentration the trade-off between stability and mobility will be. Such tests require pulsed PVD tests on targets with higher indium concentrations. At least, in the devices that are formed with pure spinel obtained from In/Ga/Zn = 1:1:1 targets, the performance shows that high channel mobilities can be obtained with pure spinel channels, despite the fact that spinel has a clear polycrystalline morphology. Our DFT simulations found a smaller m^* for monocrystalline IGZO in the spinel phase, compared to the hexagonal phase. This is only a first-order indication for increased electron mobility since phonon scattering and impurity scattering are not considered. Moreover, grain boundaries in polycrystalline materials are expected to cause electron scattering, reducing mobility as is the case in the polycrystalline hexagonal IGZO.[30,37] Such a scattering should be dominant to other potential barriers above the conduction band minimum that limits the carrier transport in IGZO.[2] Therefore, it would be interesting to explore the relationship between Hall mobility, carrier density, and temperature to compare the details of carrier transport of spinel IGZO to CAAC- and a-IGZO. Hall mobility measurements have not been explored by us yet. Instead, we preferred to demonstrate the electrical functionality more pragmatically by direct integration into scaled devices, realizing that ultimate performance might be compromised by the nonoptimized deposition or integration of CAAC- and a-IGZO. The spread in channel mobilities in Figure 10b indicates local non-uniformity problems and emphasizes the need for further focus on integrating the spinel material into scaled devices to obtain the ultimate performance of spinel IGZO and to benchmark it to CAAC- and a-IGZO. Also, reliability problems like grain boundary-induced leakage as is observed in polycrystalline semiconductors should be further investigated for spinel IGZO.

CONCLUSIONS

In summary, it is shown that IGZO in the spinel phase, free from amorphous or other known crystalline phases, can be obtained with PVD, using a spinel GZO template. The indium concentration exceeds those found in high-temperature phase diagram studies and are matching with the lattice constants as were found by DFT calculations. Using the PVD conditions as reported here shows the spinel IGZO to be a metastable phase in competition with CAAC-IGZO as is also confirmed by our DFT calculations. Those calculations also show a slightly lower effective electron mass, suggesting better electron mobility as is indicated by the improved I_{on} for TFT devices. A method to

https://doi.org/10.1021/acsaelm.1c01315
ACS Appl. Electron. Mater. 2022, 4, 1238−1249

enable the integration of spinel IGZO in front-gated devices is demonstrated. Spinel IGZO is an interesting candidate for further improving scaled TFT devices while keeping the oxygen vacancy formation under control.

■ ASSOCIATED CONTENT

Supporting Information

The Supporting Information is available free of charge at https://pubs.acs.org/doi/10.1021/acsaelm.1c01315.

Detailed composition data for IGZO at different deposition parameters; XRD spectra of spinel IGZO with variable process conditions (R_{O_2} and p-DC power); method for field-effect mobility calculations; computational details CP2K calculations; computational details Abinit calculations; and calculated energy band diagrams (PDF)

Structure file of the model used for hexagonal IGZO (CIF)

Structure file of the model used for spinel IGZO configuration 1 (CIF)

Structure file of the model used for spinel IGZO configuration 2 (CIF)

Structure file of the model used for spinel IGZO configuration 3 (CIF)

Structure file of the model used for spinel IGZO configuration 4 (CIF)

Structure file of the model used for spinel IGZO configuration 5 (CIF)

Structure file of the model used for spinel IGZO configuration 6 (CIF)

Structure file of the model used for spinel IGZO configuration 7 (CIF)

■ AUTHOR INFORMATION

Corresponding Author

Hendrik F. W. Dekkers − *IMEC, B-3001 Leuven, Belgium;* orcid.org/0000-0003-4778-5709; Email: Harold.Dekkers@imec.be

Authors

Michiel J. van Setten − *IMEC, B-3001 Leuven, Belgium; ETSF, European Theoretical Spectroscopy Facility, 91128 Palaiseau, France*

Attilio Belmonte − *IMEC, B-3001 Leuven, Belgium*

Adrian V. Chasin − *IMEC, B-3001 Leuven, Belgium*

Subhali Subhechha − *IMEC, B-3001 Leuven, Belgium*

Nouredine Rassoul − *IMEC, B-3001 Leuven, Belgium*

Anastasia V. Glushkova − *IMEC, B-3001 Leuven, Belgium; ESAT, Katholieke Universiteit, B-3001 Leuven, Belgium;* orcid.org/0000-0001-7191-6217

Romain Delhougne − *IMEC, B-3001 Leuven, Belgium*

Gouri Sankar Kar − *IMEC, B-3001 Leuven, Belgium*

Complete contact information is available at: https://pubs.acs.org/10.1021/acsaelm.1c01315

Notes

The authors declare no competing financial interest.

■ REFERENCES

(1) Petti, L.; Münzenrieder, N.; Vogt, C.; Faber, H.; Büthe, L.; Cantarella, G.; Bottacchi, F.; Anthopoulos, T. D.; Tröster, G. Metal oxide semiconductor thin-film transistors for flexible electronics. *Appl. Phys. Rev.* **2016**, *3*, No. 021303.

(2) Kamiya, T.; Nomura, K.; Hosono, H. Origins of high mobility and low operation voltage of amorphous oxide TFTs: electronic structure, electron transport, defects and doping. *J. Disp. Technol.* **2009**, *5*, 273−288.

(3) Yamazaki, S.; Ohshita, S.; Oota, M.; Baba, H.; Onuki, T.; Kunitake, H.; Ohshima, K.; Shimada, D.; Kimura, H.; Murakawa, T.; Atsumi, T.; Kato, K. Crystalline IGZO ceramics (crystalline oxide semiconductor) based devices for artificial intelligence. *Int. J. Ceram. Eng. Sci.* **2019**, *1*, 6−20.

(4) Nomura, K.; Ohta, H.; Ueda, K.; Kamiya, T.; Hirano, M.; Hosono, H. Thin-fFilm transistor fabricated in single-crystalline transparent oxide semiconductor. *Science* **2003**, *300*, 1269−1272.

(5) Orita, M.; Takeuchi, M.; Sakai, H.; Tanji, H. New transparent conductive oxides with $YbFe_2O_4$ structure. *Jpn. J. Appl. Phys.* **1995**, *34*, L1550−L1552.

(6) Nomura, K.; Ohta, H.; Takagi, A.; Kamiya, T.; Hirano, M.; Hosono, H. Room-temperature fabrication of transparent flexible thin-film transistors using amorphous oxide semiconductors. *Nature* **2004**, *432*, 488−492.

(7) Nomura, K.; Takagi, A.; Kamiya, T.; Ohta, H.; Hirano, M.; Hosono, H. Amorphous oxide semiconductors for high-performance flexible thin-Film transistors. *Jpn. J. Appl. Phys.* **2006**, *45*, 4303−4308.

(8) Van Setten, M. J.; Dekkers, H. F. W.; Kljucar, L.; Mitard, J.; Pashartis, C.; Subhechha, S.; Rassoul, N.; Delhougne, R.; Kar, G. S.; Pourtois, G. Oxygen defect stability in amorphous, C-axis aligned, and spinel IGZO. *ACS Appl. Electron. Mater.* **2021**, *3*, 4037−4046.

(9) Orita, M.; Ohta, H.; Hirano, M.; Narushima, S.; Hosono, H. Amorphous transparent conductive oxide $InGaO_3(ZnO)_m$ (m=4): a Zn4s conductor. *Philos. Mag. B* **2001**, *81*, 501−515.

(10) Suresh, A.; Gollakota, P.; Wellenius, P.; Dhawan, A.; Muth, J. F. Transparent, high mobility InGaZnO thin films deposited by PLD. *Thin Solid Films* **2008**, *516*, 1326−1329.

(11) Chen, W. T.; Lo, S. Y.; Kao, S. C.; Zan, H. W.; Tsai, C. C.; Lin, J. H.; Fang, C. H.; Lee, C. C. Oxygen-dependent instability and annealing/passivation effects in amorphous In-Ga-Zn-O thin-film transistors. *IEEE Electron Device Lett.* **2011**, *32*, 1552−1554.

(12) Orita, M.; Tanji, H.; Mizuno, M.; Adachi, H.; Tanaka, I. Mechanism of electrical conductivity of transparent $InGaZnO_4$. *Phys. Rev. B* **2000**, *61*, 1811−1816.

(13) Kimizuka, N.; Mohri, T. Spinel, $YbFe_2O_4$, and $Yb_2Fe_3O_7$ types of structures for compounds in the In_2O_3 and Sc_2O_3-A_2O_3-BO systems [A: Fe, Ga, or Al; B: Mg, Mn, Fe, Ni, Cu, or Zn] at temperatures over 1000 °C. *J. Solid State Chem.* **1985**, *60*, 382−384.

(14) Nakamura, M.; Kimizuka, N.; Mohri, T. The phase relations in the In_2O_3-Ga_2ZnO_4-ZnO systems at 1350 °C. *J. Solid State Chem.* **1991**, *93*, 298−315.

(15) Haeberle, J.; Brizzi, S.; Gaspar, D.; Barquinha, P.; Galazka, Z.; Schulz, D.; Schmeißer, D. A spectroscopic comparison of IGZO thin films and the parent In_2O_3, Ga_2O_3, and ZnO single crystals. *Mater. Res. Express* **2016**, *3*, No. 106302.

(16) Nomura, K.; Kamiya, T.; Ohta, H.; Uruga, T.; Hirano, M.; Hosono, H. Local coordination structure and electronic structure of the large electron mobility amorphous oxide semiconductor In-Ga-Zn-O: Experiment and ab initio calculations. *Phys. Rev. B* **2007**, *75*, No. 035212.

(17) Schmeißer, D.; Haeberle, J. Intrinsic localized gap states in IGZO and its parent single crystalline TCOs. *Thin Solid Films* **2016**, *603*, 206−211.

(18) Troughton, J.; Atkinson, D. Amorphous InGaZnO and metal oxide semiconductor devices: an overview and current status. *J. Mater. Chem. C* **2019**, *7*, 12388−12414.

(19) Seo, D. K.; Shin, S.; Cho, H. H.; Kong, B. H.; Whang, D. M.; Cho, H. K. Drastic improvement of oxide thermoelectric performance using thermal and plasma treatments of the InGaZnO thin films grown by sputtering. *Acta Mater.* **2011**, *59*, 6743−6750.

(20) Cho, S. W.; Baek, S. K.; Kim, D. E.; Kim, Y.; Choa, H. K. Microstructure-dependent thermoelectric properties of polycrystalline

$InGaO_3(ZnO)_2$ superlattice films. *J. Vac. Sci. Technol., A* **2017**, *35*, No. 01B126.
(21) Lee, W.-J.; Choi, E.-A.; Bang, J.; Ryu, B.; Chang, K. J. Structural and electronic properties of crystalline $InGaO_2(ZnO)_m$. *Appl. Phys. Lett.* **2008**, *93*, No. 111901.
(22) Liang, X.; Clarke, D. R. Single layer In-O atomic sheets as phonon and electron barriers in ZnO-In_2O_3 natural superlattices: Implications for thermoelectricity. *J. Appl. Phys.* **2018**, *124*, No. 025101.
(23) Tanaka, Y.; Wada, K.; Kobayashi, Y.; Fujii, T.; Denholme, S. J.; Sekine, R.; Kase, N.; Kimizuka, N.; Miyakawa, N. Single crystal growth of bulk $InGaZnO_4$ and analysis of its intrinsic transport properties. *CrystEngComm* **2019**, *21*, 2985−2993.
(24) Yamazaki, S.; Suzawa, H.; Inoue, K.; Kato, K.; Hirohashi, T.; Okazaki, K.; Kimizuka, N. Low turn-on voltage due to conduction band lowering effect in crystalline indium gallium zinc oxide transistors. *Jpn. J. Appl. Phys.* **2014**, *53*, No. 04ED18.
(25) Waseda, Y.; Sugiyama, K.; Kawamata, T. Nanometer-sized crystalline clusters of IGZO films determined from the grazing incidence x-ray scattering and anomalous x-ray scattering data combined with Reverse monte Carlo simulations. *Mater. Trans.* **2018**, *59*, 1691−1700.
(26) Yamazaki, S.; Ohshita, S.; Oota, M.; Baba, H.; Onuki, T.; Kunitake, H.; Ohshima, K.; Shimada, D.; Kimura, H.; Murakawa, T.; Atsumi, T.; Kato, K. Crystalline IGZO ceramics (crystalline oxide semiconductor)-based devices for artificial intelligence. *Int. J. Ceram. Eng. Sci.* **2019**, *1*, 6−20.
(27) Kimizuka, N.; Yamazaki, S. *Physics and Technology of Crystalline Oxide, Semiconductor CAAC-IGZO: Fundamentals*; Wiley, 2017; pp 54−70.
(28) Lynch, D. M.; Zhu, B.; Levin, B. D. A.; Muller, D. A.; Ast, D. G.; Greene, R. G.; Thompson, M. O. Characterization of reactively sputtered c-axis aligned nanocrystalline $InGaZnO_4$. *Appl. Phys. Lett.* **2014**, *105*, No. 262103.
(29) Ahn, B. D.; Shing, H. S.; Kim, D. L.; Lee, S. M.; Park, J.-S.; Kim, G. H.; Kim, H. Origin of device performance degradation in InGaZnO thin-film transistors after crystallization. *J. Jpn. J. Appl. Phys.* **2012**, *51*, No. 015601.
(30) Suko, A.; Jia, J.; Nakamura, S.; Kawashima, E.; Utsuno, F.; Yano, K.; Shigesato, Y. Crystallization behavior of amorphous indium−gallium−zinc-oxide films and its effects on thin-film transistor performance. *Jpn. J. Appl. Phys.* **2016**, *55*, No. 035504.
(31) Hiramatsu, T.; Nakashima, M.; Kikuchi, E.; Ishihara, N.; Tsubuku, M.; Dairiki, K.; Yamazaki, S. Correlation between crystallinity and oxygen vacancy formation in In−Ga−Zn oxide. *Jpn. J. Appl. Phys.* **2016**, *55*, No. 021203.
(32) Asami, Y.; Kurata, M.; Okazaki, Y.; Higa, E.; Matsubayashi, D.; Okamoto, S.; Sasagawa, S.; Moriwaka, T.; Kakehata, T.; Yakubo, Y.; Kato, K.; Hamada, T.; Sakakura, M.; Hayakawa, M.; Yamazaki, S. Properties of c-axis-aligned crystalline indium−gallium−zinc oxide field-effect transistors fabricated through a tapered-trench gate process. *Jpn. J. Appl. Phys.* **2016**, *55*, No. 04EG09.
(33) Obonai, T.; Okazaki, K.; Hosaka, Y.; Yamazaki, S. Relation between crystallinity and constituent distribution of an IGZO thin film. *Jpn. J. Appl. Phys.* **2019**, *58*, No. 091003.
(34) Zhu, B.; Roach, K. E.; Lynch, D. M.; Chung, C.-Y.; Ast, D. G.; Greene, R. G.; Thompson, M. O. Effects of RF sputtering parameters on C-axis aligned crystalline (CAAC) $InGaZnO_4$ films using design of experiment (DOE) approach. *ECS J. Solid State Sci. Technol.* **2016**, *5*, P368−P375.
(35) Ide, K.; Nomura, K.; Hiramatsu, H.; Kamiya, T.; Hosono, H. Structural relaxation in amorphous oxide semiconductor, a-In-Ga-Zn-O. *J. Appl. Phys.* **2012**, *111*, No. 073513.
(36) Shimomura, A.; Koyama, M.; Ishiyama, T.; Ohta, M.; Tsubuku, M.; Kikuchi, E.; Hirohashi, T.; Takahashi, M.; Yamazaki, S. In *Crystallography of Excimer Laser-Crystallized In−Ga−Zn−O Film*, Proceedings of 2013 Twentieth International Workshop on Active-Matrix Flatpanel Displays and Devices (AM-FPD); IEEE, 2013; pp 155−158.
(37) Park, K.; Park, H.-W.; Shin, H. S.; Bae, J.; Park, K.-S.; Kang, I.; Chung, K.-B.; Kwon, J.-Y. Reliability of crystalline Indium−Gallium−Zinc-Oxide thin-film transistors under bias stress with light illumination. *IEEE Trans. Electron Devices* **2015**, *62*, 2900−2905.
(38) Glushkova, A. V.; Dekkers, H. F. W.; Nag, M.; Del Agua Borniquel, J.; Ramalingam, J.; Genoe, J.; Heremans, P.; Rolin, C. Systematic study on the amorphous, C-axis-aligned crystalline, and protocrystalline phases in In−Ga−Zn 0xide thin-film fransistors. *ACS Appl. Electron. Mater.* **2021**, *3*, 1268−1278.
(39) Galazka, Z.; Ganschow, S.; Schewski, R.; Irmscher, K.; Klimm, A.; Kwasniewski, D.; Pietsch, M.; Fiedler, A.; Schulze-Jonack, I.; Albrecht, M.; Schröder, T.; Bickermann, M. Ultra-wide bandgap, conductive, high mobility, and high quality melt-grown bulk $ZnGa_2O_4$ single crystals. *APL Mater.* **2019**, *7*, No. 022512.
(40) Belmonte, A.; Oh, H.; Rassoul, N.; Donadio, G.; Mitard, J.; Dekkers, H.; Delhougne, R.; Subhechha, S.; Chasin, A.; van Setten, M. J.; Kljucar, L.; Mao, M.; Puliyalil, H.; Pak, M.; Teugels, L.; Tsvetanova, D.; Banerjee, K.; Souriau, L.; Tokei, Z.; Goux, L.; Kar, G. S. In *Capacitor-Less, Long-Retention (>400s) DRAM Cell Paving the Way towards Low-Power and High-Density Monolithic 3D DRAM*, 2020 IEEE International Electron Devices Meeting (IEDM), 2020; pp 28.2.1−28.2.4.
(41) Nakamura, M.; Kimizuka, N.; Mohri, T.; Isobe, M. Phase equilibria in the system In_2O_3-M_2ZnO_4-ZnO at 1350 °C (M=Fe, Ga, AI) and crystal chemical consideration of $InMO_3(ZnO)_m$ phases with $LuFeO_3(ZnO)_m$-type structures. *J. Alloys Compd.* **1993**, *192*, 105−107.
(42) Hohenberg, P.; Kohn, W. Inhomogeneous electron gas. *Phys. Rev. B* **1964**, *136*, B864−B871.
(43) Kohn, W.; Sham, L. J. Self-consistent equations including exchange and correlation effects. *Phys. Rev. A* **1965**, *140*, A1133−A1138.
(44) Lejaeghere, K.; Bihlmayer, G.; Björkman, T.; Blaha, P.; Blügel, S.; Blum, V.; Caliste, D.; Castelli, I. E.; Clark, S. J.; Dal Corso, A.; de Gironcoli, S.; Deutsch, T.; Dewhurst, J. K.; Di Marco, I.; Draxl, C.; Dułak, M.; Eriksson, O.; Flores-Livas, J. A.; Garrity, K. F.; Genovese, L.; Giannozzi, P.; Giantomassi, M.; Goedecker, S.; Gonze, X.; Grånäs, O.; Gross, E. K. U.; Gulans, A.; Gygi, F.; Hamann, D. R.; Hasnip, P. J.; Holzwarth, N. A.; Iuşan, D.; Jochym, D. B.; Jollet, F.; Jones, D.; Kresse, G.; Koepernik, K.; Küçükbenli, E.; Kvashnin, Y. O.; Locht, I. L.; Lubeck, S.; Marsman, M.; Marzari, N.; Nitzsche, U.; Nordström, L.; Ozaki, T.; Paulatto, L.; Pickard, C. J.; Poelmans, W.; Probert, M. I.; Refson, K.; Richter, M.; Rignanese, G. M.; Saha, S.; Scheffler, M.; Schlipf, M.; Schwarz, K.; Sharma, S.; Tavazza, F.; Thunström, P.; Tkatchenko, A.; Torrent, M.; Vanderbilt, D.; van Setten, M. J.; Van Speybroeck, V.; Wills, J. M.; Yates, J. R.; Zhang, G. X.; Cottenier, S. Reproducibility in density functional theory calculations of solids. *Science* **2016**, *351*, No. add3000.
(45) Perdew, J. P.; Burke, K.; Ernzerhof, M. Generalized gradient approximation made simple. *Phys. Rev. Lett.* **1996**, *77*, 3865−3868.
(46) Perdew, J. P.; Ruzsinszky, A.; Csonka, G. I.; Vydrov, O. A.; Scuseria, G. E.; Constantin, L. A.; Zhou, X.; Burke, K. Restoring the density-gradient expansion for exchange in solids and surfaces. *Phys. Rev. Lett.* **2008**, *100*, No. 136406.
(47) Kühne, T. D.; Iannuzzi, M.; Del Ben, M.; Rybkin, V. V.; Seewald, P.; Stein, F.; Laino, T.; Khaliullin, R. Z.; Schütt, O.; Schiffmann, F.; Golze, D.; Wilhelm, J.; Chulkov, S.; Bani-Hashemian, M. H.; Weber, V.; Borčtnik, U.; Taillefumier, M.; Jakobovits, A. S.; Lazzaro, A.; Pabst, H.; Müller, T.; Schade, R.; Guidon, M.; Andermatt, S.; Holmberg, N.; Schenter, G. K.; Hehn, A.; Bussy, A.; Belleflamme, F.; Tabacchi, G.; Glöß, A.; Lass, M.; Bethune, I.; Mundy, C. J.; Plessl, C.; Watkins, M.; VandeVondele, J.; Krack, M.; Hutter, J. CP2K: An electronic structure and molecular dynamics software package - Quickstep: Efficient and accurate electronic structure calculations. *J. Chem. Phys.* **2020**, *152*, No. 194103.
(48) Gonze, X.; Jollet, F.; Araujo, F. A.; Adams, D.; Amadon, B.; Applencourt, T.; Audouze, C.; Beuken, J.-M.; Bieder, J.; Bokhanchuk, A.; Bousquet, E.; Bruneval, F.; Caliste, D.; Côté, M.; Dahm, F.; Pieve, F. D.; Delaveau, M.; Gennaro, M. D.; Dorado, B.; Espejo, C.;

https://doi.org/10.1021/acsaelm.1c01315
ACS Appl. Electron. Mater. 2022, 4, 1238−1249

Geneste, G.; Genovese, L.; Gerossier, A.; Giantomassi, M.; Gillet, Y.; Hamann, D.; He, L.; Jomard, G.; Janssen, J. L.; Roux, S. L.; Levitt, A.; Lherbier, A.; Liu, F.; Lukacevicc, I.; Martin, A.; Martins, C.; Oliveira, M.; Poncé, S.; Pouillon, Y.; Rangel, T.; Rignanese, G.-M.; Romero, A.; Rousseau, B.; Rubel, O.; Shukri, A.; Stankovski, M.; Torrent, M.; van Setten, M. V.; Troeye, B. V.; Verstraete, M.; Waroquiers, D.; Wiktor, J.; Xu, B.; Zhou, A.; Zwanziger, J. W. Recent developments in the ABINIT software package. *J. Comput. Phys. Commun.* **2016**, *205*, 106−131.

(49) Gonze, X.; Amadon, B.; Antonius, G.; Arnardi, F.; Baguet, L.; Beuken, J.-M.; Bieder, J.; Bottin, F.; Bouchet, J.; Bousquet, E.; Brouwer, N.; Bruneval, F.; Brunin, G.; Cavignac, T.; Charraud, J.-B.; Chen, W.; Côté, M.; Cottenier, S.; Denier, J.; Geneste, G.; Ghosez, P.; Giantomassi, M.; Gillet, Y.; Gingras, O.; Hamann, D. R.; Hautier, G.; He, X.; Helbig, N.; Holzwarth, N.; Jia, Y.; Jollet, F.; Lafargue-Dit-Hauret, W.; Lejaeghere, K.; Marques, M. A.; Martin, A.; Martins, C.; Miranda, H. P.; Naccarato, F.; Persson, K.; Petretto, G.; Planes, V.; Pouillon, Y.; Prokhorenko, S.; Ricci, F.; Rignanese, G.-M.; Romero, A. H.; Schmitt, M. M.; Torrent, M.; van Setten, M. J.; Troeye, B. V.; Verstraete, M. J.; Zérah, G. Z.; Zwanziger, J. W. The Abinit project: Impact, environment and recent developments. *Comput. Phys. Commun.* **2020**, *248*, No. 107042.

(50) Romero, A. H.; Allan, D. C.; Amadon, B.; Antonius, G.; Applencourt, T.; Baguet, L.; Bieder, J.; Bottin, F.; Bouchet, J.; Bousquet, E.; Bruneval, F.; Brunin, G.; Caliste, D.; Côté, M.; Denier, J.; Dreyer, C.; Ghosez, P.; Giantomassi, M.; Gillet, Y.; Gingras, O.; Hamann, D. R.; Hautier, G.; Jollet, F.; Jomard, G.; Martin, A.; Miranda, H. P. C.; Naccarato, F.; Petretto, G.; Pike, N. A.; Planes, V.; Prokhorenko, S.; Rangel, T.; Ricci, F.; Rignanese, G.-M.; Royo, M.; Stengel, M.; Torrent, M.; van Setten, M. J.; Troeye, B. V.; Verstraete, M. J.; Wiktor, J.; Zwanziger, J. W.; Gonze, X. ABINIT: Overview and focus on selected capabilities. *J. Chem. Phys.* **2021**, *152*, No. 124102.

(51) Van Setten, M. J.; Giantomassi, M.; Bousquet, E.; Verstraete, M. J.; Hamann, D. R.; Gonze, X.; Rignanese, G.-M. The PseudoDojo: Training and grading a 85 element optimized norm-conserving pseudopotential table. *Comput. Phys. Commun.* **2018**, *226*, 39−54.

(52) Haas, P.; Tran, F.; Blaha, P. Calculation of the lattice constant of solids with semilocal functionals. *Phys. Rev. B* **2009**, *79*, No. 085104.

(53) Marezio, M. Refinement of the crystal structure of In_2O_3 at two wavelengths. *Acta Crystallogr.* **1966**, *20*, 723−728. and JCPDS card #06-0416.

(54) Hill, R. J.; Graig, J. R.; Gibbs, G. V. Systematics of the spinel structure type. *Phys. Chem. Miner.* **1979**, *4*, 317−339. and Inorganic Crystal Structure Database. ICSD 81105. http://www.fiz-karlsruhe.de/icsd.html (retrieved Oct 10, 2021).

(55) Olziersky, A.; Barquinhab, P.; Vilà, A.; Magaña, C.; Fortunato, E.; Morantea, J. R.; Martins, R. Role of Ga2O3−In2O3−ZnO channel composition on the electrical performance of thin-film transistors. *Mater. Chem. Phys.* **2011**, *131*, 512−518.

(56) Zinkevich, M.; Morales, F. M.; Nitsche, H.; Ahrens, M.; Ruhle, M.; Aldinger, F. Microstructural and Thermodynamic Study of γ-Ga2O3. *Z. Metallkd.* **2004**, *95*, 756−762.

(57) Playford, H. Y.; Hannon, A. C.; Tucker, M. G.; Dawson, D. M.; Ashbrook, S. E.; Kastiban, R. J.; Sloan, J.; Walton, R. I. Characterization of structural disorder in γ-Ga2O3. *J. Phys. Chem. C* **2014**, *118*, 16188−16198.

(58) Seko, A.; Yuge, K.; Oba, F.; Kuwabara, A.; Tanaka, I. Prediction of ground-state structures and order-disorder phase transitions in II-III spinel oxides: A combined cluster-expansion method and first-principles study. *Phys. Rev. B* **2006**, *73*, No. 184117.

(59) Ast, D. G. IGZO and a-Si:H: A topological constraint theory view. *ECS Trans.* **2017**, *79*, 59−68.

(60) Mráz, S.; Schneider, J. M. Influence of the negative oxygen ions on the structure evolution of transition metal oxide thin films. *J. Appl. Phys.* **2006**, *100*, No. 023503.

(61) Jia, J.; Torigoshi, Y.; Shigesatoa, Y. In situ analyses on negative ions in the indium-gallium-zinc oxide sputtering process. *Appl. Phys. Lett.* **2013**, *103*, No. 013501.

https://doi.org/10.1021/acsaelm.1c01315
ACS Appl. Electron. Mater. 2022, 4, 1238−1249